

Kinetics-Driven Crystal Facets Evolution at the Tip of Nanowires: A New Implementation of the Ostwald-Lussac Law

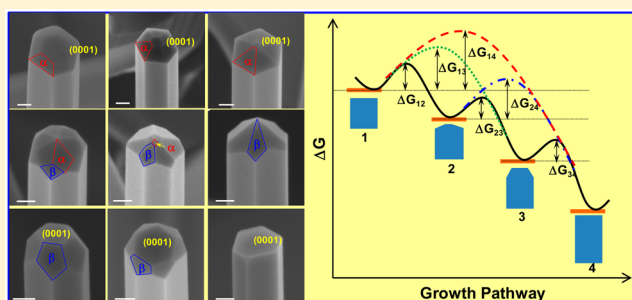
Xin Yin and Xudong Wang*

Department of Materials Science and Engineering, University of Wisconsin-Madison, Madison, Wisconsin 53706, United States

S Supporting Information

ABSTRACT: Nanocrystal facets evolution is critical for designing nanomaterial morphology and controlling their properties. In this work, we report a unique high-energy crystal facets evolution phenomenon at the tips of wurtzite zinc oxide nanowires (NWs). As the zinc vapor supersaturation decreased at the NW deposition region, the NW tip facets evolved from the (0001) surface to the {10 $\bar{1}$ 3} surface and subsequently to the {11 $\bar{2}$ 2} surface and eventually back to the flat (0001) surface. A series of NW tip morphology was observed in accordance to the different combinations of exposed facets. Exposure of the high-energy facets was attributed to the fluctuation of the energy barriers for the formation of different crystal facets during the layer-by-layer growth of the NW tip. The energy barrier differences between these crystal facets were quantified from the surface area ratios as a function of supersaturation. On the basis of the experimental observation and kinetics analysis, we argue that at appropriate deposition conditions exposure of the crystal facets at NW growth front is not merely determined by the surface energy. Instead, the NW may choose to expose the facets with minimal formation energy barrier, which can be determined by the Ehrlich-Schwoebel barrier variation. This empirical law for the NW tip facet formation was in analogy to the Ostwald-Lussac law of phase transformation, which brings a new insight toward nanostructure design and controlled synthesis.

KEYWORDS: Nanowire growth, crystal facets evolution, Ostwald-Lussac law, kinetics control, supersaturation



Controlled growth of crystals is crucial to designing and obtaining the extraordinary physical, chemical, electronic, and mechanical properties of nanomaterials.^{1–3} Among many endeavors toward controlled synthesis of nanostructures, manipulating the crystal facets has been one of the most intensively studied aspects in materials science. Because of the distinguishing chemical activity on different facets, the exposed crystal facets are always the dominating factor that determines the materials' geometry, catalytic activity, structural stability, and toxicity.^{4–7} In principle, a stable crystal system tends to expose the facets with the lowest surface energy. For example, metal nanoparticles with a face-centered cubic lattice, such as Au and Pt, typically exhibit a truncated-octahedron shape exposing their {111} and {100} facets.^{8,9} Rutile TiO₂, a common paint and catalytic material, typically shows a rectangular geometry covered by the {001} and {110} facets.¹⁰ Wurtzite nanocrystals, such as ZnO, ZnS, and GaN, are usually dominated by the hexagonal rod or plate shapes constructed by the {0001} and {01 $\bar{1}$ 0} facets.^{11,12} Ideally, the equilibrium morphology of nanocrystals can be predicted by the Wolf's theorem, which uses the surface energy as the only measure to determine the exposed facets and their relative sizes.¹³ In reality, the synthesized nanocrystals exhibited splendid morphologies that are far beyond what the theory can predict thermodynamically. High-energy surfaces are not rare to find in many nanostructures.^{14,15} Their appearances are essential for

the nanomaterials to exhibit extraordinary properties and have tremendous practical values, such as design of advanced catalytic materials.^{16–18} Nevertheless, there are many kinetic factors that influence the crystal facet evolution. Understanding and implementation of the kinetic factors are still in the very premature stage. The most broadly practiced strategy is to introduce selective adsorption of capping agents to obtain nanocrystals with high energy facets through solution-based methods.^{9,19} While high-temperature vapor-based approaches have been applied to the growth of many advanced nanomaterials, little is known about the kinetics-controlling crystal facets evolution under nonequilibrium conditions. Our recent kinetics study on crystal growth evidenced a layer-by-layer growth model for quasi one-dimensional (1D) nanowires (NWs) and two-dimensional (2D) nanoplates.^{20,21} It revealed a significant role of supersaturation in controlling the nanostructure morphology evolution. In this paper, we present that the layer-by-layer growth of ZnO NWs also induces an intriguing kinetic factor that controls the combination of crystal facets at the growth front. The appearance of metastable high-energy facets is attributed to the lower formation transition energy barrier. This phenomenon is analogical to the Ostwald-Lussac

Received: August 7, 2016

Revised: October 3, 2016

Published: October 19, 2016

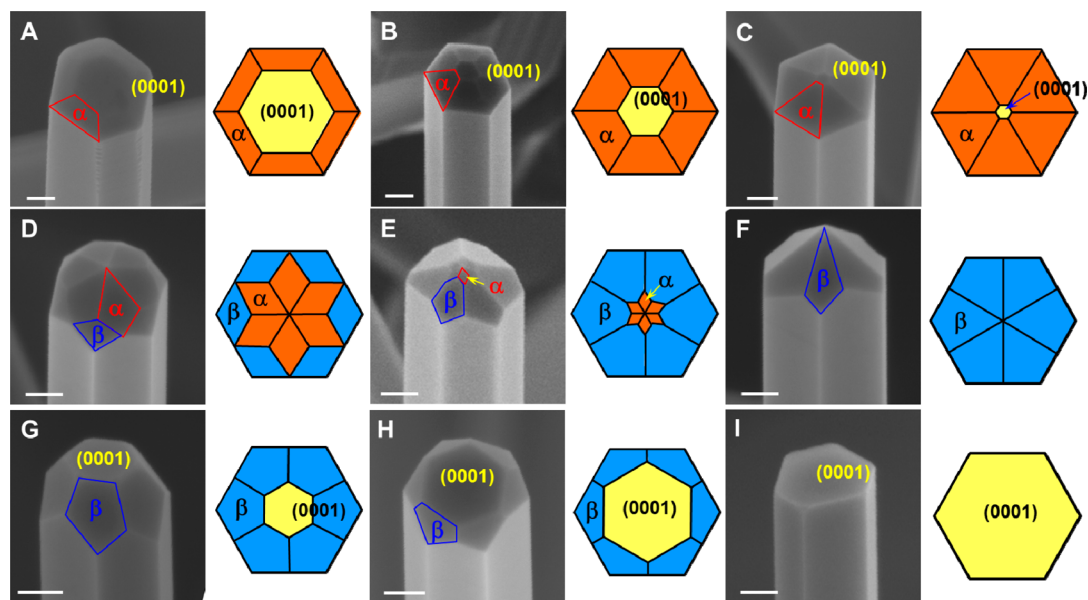


Figure 1. SEM images and corresponding schematic showing facets evolution at NW tips. (A–C) NW with the tip enclosed by six α -facets and one facet (0001). From (A–C), facet (0001) gradually decreased when facets α increased simultaneously. (D–F) NW with the tip covered by six α -facets and six β -facets. From (D–F), facets β appeared, expanded, and eventually covered the entire tip area at the expenses of facets α . (G–I) NW with six β -facets and one (0001) facet coexisted tip. From (G–I), facets β gradually vanished and facet (0001) appeared again with a 30° rotation relative to the six sidewall of the NW. In the schematic, yellow represents facet (0001), orange is facet α , and blue is facet β . All scale bars are 100 nm.

(OL) law of phase transformation,^{22–24} which states that an unstable system tends to transform into one phase with minimum energy loss. This new insight of crystal facet evolution kinetics in NW growth will bring significant value toward nanostructure design and controlled synthesis. In addition, control of NW tip morphology also possesses great potential in many NW-based applications, such as high-resolution scanning probe and nanoelectrodes.^{25,26}

ZnO NWs were grown through a dynamically controlled vapor–solid deposition process (see Experimental Process in Supporting Information S1.1). During the NW growth, both the evaporation temperature and the deposition temperature were steadily increased in order to achieve a continuously increased vapor concentration during the NW growth. Under such a nonsteady state deposition condition, randomly oriented submicron-sized ZnO NWs were grown on the polycrystalline alumina substrate within a broad temperature range from 1300 to 1673 K (Figure S1A). The NWs were typically 20 μm long with a diameter of ~ 300 nm. Most NWs exhibited a clear hexagonal cross section due to the $P6_3mc$ lattice symmetry of the wurtzite crystal structure (Figure S1B). In order to distinguish from common ZnO NWs that typically have a flat hexagonal (0001) tip facet,^{27,28} the tips of ZnO NWs received from the dynamic deposition condition were mostly enclosed by at least two groups of crystal facets (inset of Figure S1A). These tip facets also distributed with a hexagonal symmetry. The NW tip facets evolution were only found at a high deposition temperature region (1665 K) and directly related to the deposition location. As shown by the relationship between deposition temperature and location in the deposition chamber in Figure S2, the temperature was almost constant within that region. At other deposition region, the NWs tip was the regular flat (0001) facet. Within this narrow deposition region window (~ 1 cm), different crystal facets evolved and vanished as the deposition location changed slightly.

Representative tip morphology illustrating the tip facets evolution as a function of location and corresponding schematic drawing are presented in Figure 1. Larger scale images showing NWs with the same facet configuration in nearby regions (± 1 μm) are presented in Figure S3. At the position closest to the chamber center (17.7 cm from the chamber center, where the precursor source was located), the NW's tip was only partially covered by the hexagonal (0001) facet at the center with six angled facets (named as α -facet) evenly distributed along the six edges between the vertical sidewall facet and the top (0001) facet, as shown in Figure 1A. As the deposition position moved slightly downstream by ~ 3 mm, the six α -facets gradually expanded and eventually occupied the entire tip area. Meanwhile, the (0001) facet shrank into a sharp point at the center of the tip (Figure 1A–C). Subsequently, another group of facets (named as β -facet) emerged at the six radial corners of the tips (Figure 1D). The β -facets expanded and eventually covered the entire tip area at the expense of the α -facets as the deposition position moved downstream by another ~ 3 mm (Figure 1D–F). At the position slightly farther away from the chamber center, the hexagonal (0001) facet appeared again from the center of the tip. Different from the original (0001)-faceted NWs shown in Figure 1A, however, the re-emerged (0001) facet exhibited a 30° rotation relative to the hexagonally distributed NW sidewalls (Figure 1G). This phenomenon is a result of the intersection between the six β -facets and the (0001) facet at the NW tip. The (0001) facet expanded and eventually took over the entire NW tip again at the deposition position of 18.7 cm away from the chamber center, where the β -facets vanished completely (Figure 1H,I). Across this narrow deposition region, the deposition temperature difference was negligible (< 5 $^\circ\text{C}$, Figure S2). The vapor pressure of the precursor changed significantly due to the rapid deposition across this region. These suggested that the precursor supersaturation was the dominating factor at this high-deposition temperature area. Thus, the facet evolution is

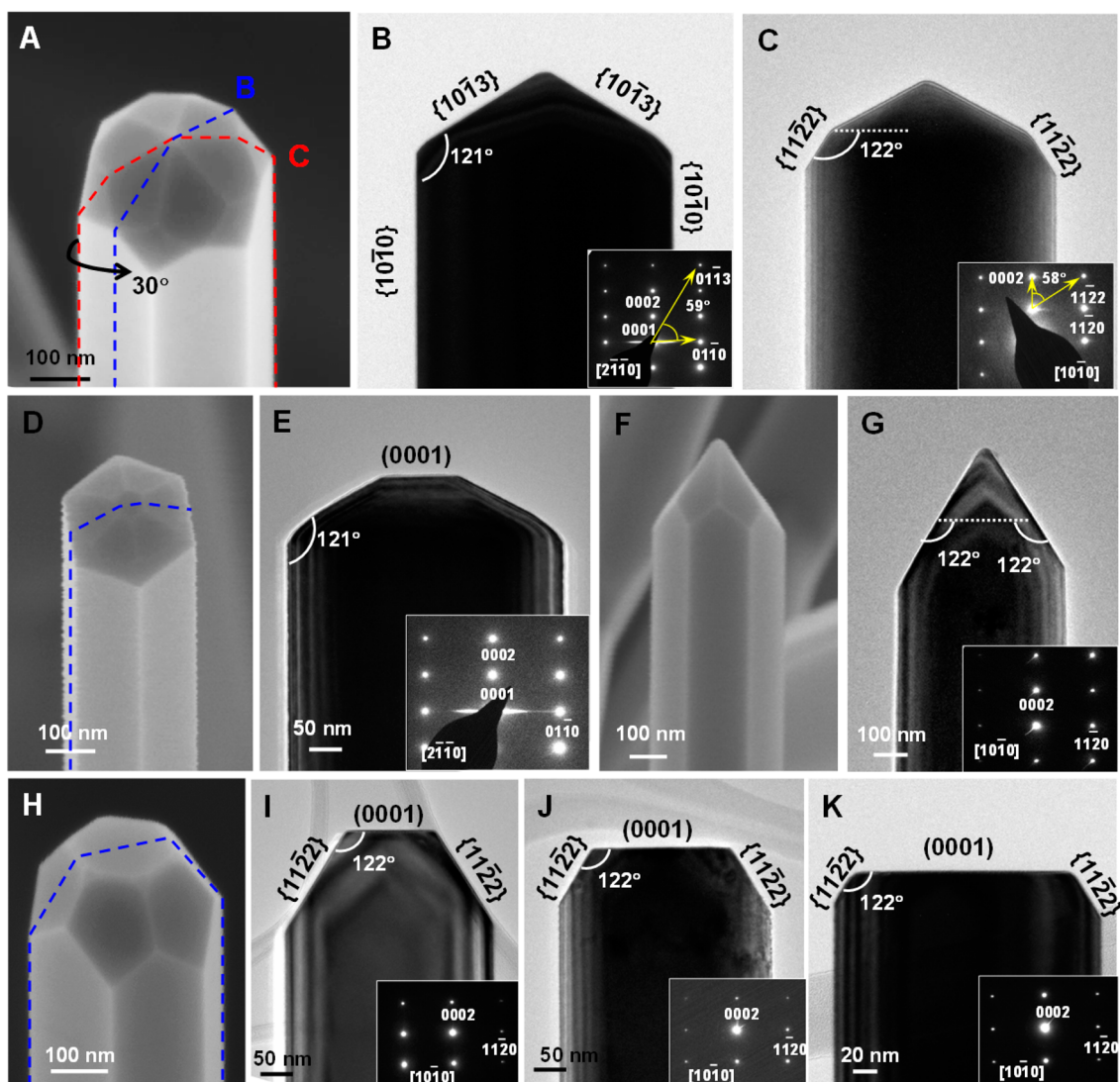


Figure 2. SEM images and TEM projections for facets indexing. (A) NW with facets $\{11\bar{2}2\}$ and facets $\{10\bar{1}3\}$ coexisted tip. TEM projection and SAED patterns (inset) along (B) the direction $[2\bar{1}10]$ and (C) the direction $[10\bar{1}0]$. (D) NW with facets $\{10\bar{1}3\}$ and facet (0001) coexisted tip and (E) the corresponding TEM projection. Inset is the SAED pattern along $[2\bar{1}10]$. (F) NW with tip totally solely covered by facets $\{11\bar{2}2\}$ and (G) corresponding TEM projection. Inset is the SAED pattern along $[10\bar{1}0]$. (H) NW with facets $\{11\bar{2}2\}$ and facet (0001) coexisted tip and (I–K) corresponding TEM projection. Insets are the SAED patterns along $[10\bar{1}0]$ showing the facets $\{11\bar{2}2\}$ and facet (0001) evolution under different supersaturation.

primarily correlated to the location-induced supersaturation difference.

In order to understand the tip facets evolution phenomenon, the involving facets were indexed first. Transmission electron microscopy (TEM) was implemented to characterize selected NW tips from various projection directions. A NW with both the α - and β -facets was imaged as shown in Figure 2A. TEM image was first recorded along the $[2\bar{1}10]$ projection direction, where only the α -facets can be seen (Figure 2B). The projection plane was also outlined by the dashed blue line in Figure 2A. Thus, the angle between the $\{10\bar{1}0\}$ and α -facets was directly measured to be 121° from the projected image, which matches well to the selective area electron diffraction (SAED) pattern (inset of Figure 2B). It is noted that in the SAED pattern the presence of the forbidden Bragg spots of the (0001) and (0003) planes was attributed to the secondary Bragg electron diffraction according to the satisfied condition (e.g., $(0\bar{1}11) + (0\bar{1}10) = (0001)$). Therefore, the α -facet was

indexed to be facets $\{10\bar{1}3\}$, a high index plane. By tilting the same NW by 30° along the NW's axial axis (the $[0001]$ direction), another projection consisting of both the α - and β -facets were imaged, as shown in Figure 2C. The SAED pattern (the inset of Figure 2C) confirmed that projection was now along the $[10\bar{1}0]$ direction. The geometry of the projected image was outlined by the dashed red line in Figure 2A. At this condition, the β -facets were parallel to the electron beam, enabling the measurement of the angle between the β -facets and the horizontal plane (known to be the (0001) plane). The angle was measured to be 122° . Therefore, from the corresponding SAED pattern (inset of Figure 2C), the β -facet was determined to be $\{11\bar{2}2\}$, another high index plane.

NWs at different evolution stages were collected to further confirm the combination of tip facets. One NW with the $\{10\bar{1}3\}$ facets coexisted with the (0001) facet at the tip was imaged and characterized (Figure 2D). A TEM image was taken from a projection plane of $[2\bar{1}10]$ (Figure 2E), as

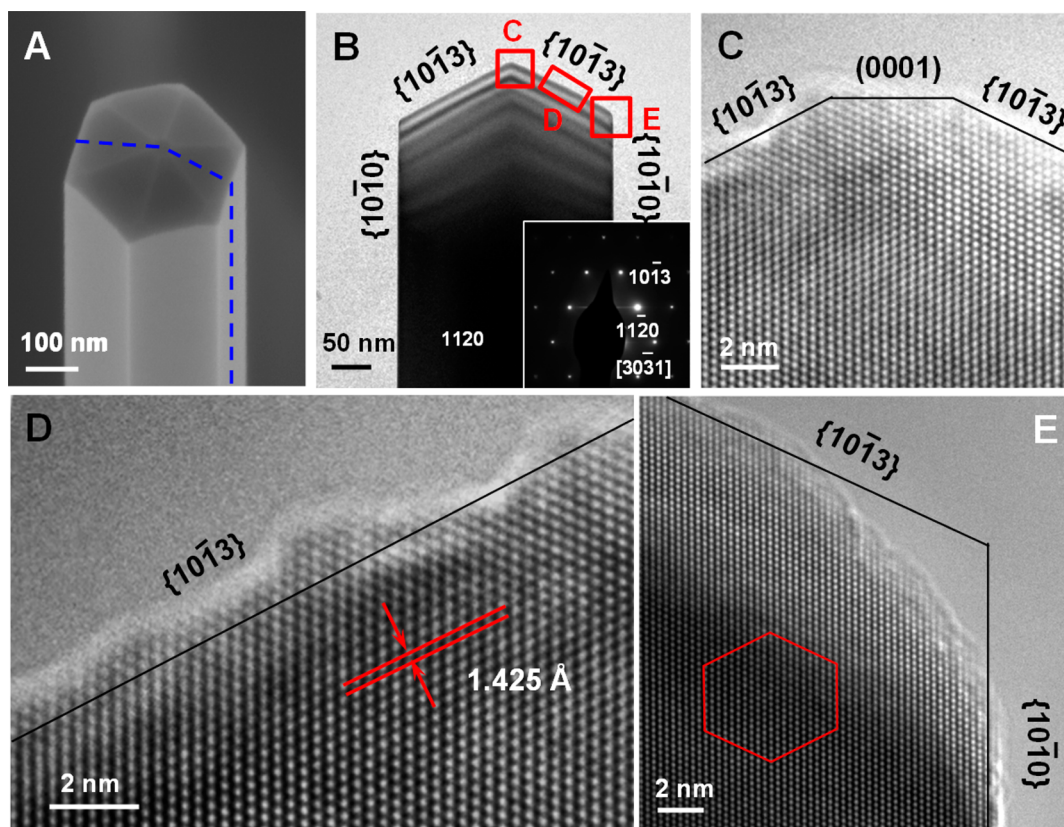


Figure 3. HRTEM images on the lattice structure at the NW tip. (A) NW with the tip predominately covered by facets $\{10\bar{1}3\}$ and (B) the corresponding TEM projection. Inset is the SAED pattern along $[30\bar{3}1]$. (C) HRTEM at the tip region, marked in (B), showing facets $\{10\bar{1}3\}$ sharp connected by a small portion of facet (0001). (D) Facet $\{10\bar{1}3\}$, marked in (B), showing the rough surface. Islands with a few atomic layer thickness covered almost the entire surface. (E) Corner between facet $\{10\bar{1}3\}$ and $\{10\bar{1}0\}$, marked in (B), showing multiatomic-layer steps, induced by the surface energy minimization.

outlined by the dashed blue line in Figure 2D. The orientation was validated by the corresponding SAED pattern (inset of Figure 2E), which was the same as the SAED pattern of the projection in Figure 2B. The angle between the $\{10\bar{1}3\}$ facet and the $\{10\bar{1}0\}$ facets was measured to be 121° , identical to that value measured in Figure 2B, confirming the same facets configuration in this NW tip. Another NW with the tip solely covered by six $\{11\bar{2}2\}$ facets (Figure 2F) was imaged along the $[10\bar{1}0]$ direction (Figure 2G). The angle between the $\{11\bar{2}2\}$ facet and the horizontal plane (dashed line, (0001)) was measured to be 122° , indicating the same facet group as those shown in Figure 2C. Another NW with the combination of $\{11\bar{2}2\}$ and (0001) facets at the tip is shown in Figure 2H. TEM image projected along the $[10\bar{1}0]$ direction is shown in Figure 2I. The angle between the flat tip and the $\{11\bar{2}2\}$ facet was measured to be 122° , identical to the measurement when the (0001) facet was not adjacent (Figure 2C). All these measurements confirmed that there were the same groups of crystal facets during the tip morphology evolution. The TEM image also showed clear thickness fringes around the NW edges. The different fringe patterns from outside to the center directly correlated to the facets organization. Other NWs obtained at the slightly lower supersaturation region had the same facets combination but larger (0001) area (Figure 2J,K). All the SAED patterns and facets angles were identical, confirming that no more new facets were evolved when the NW tip was reclaimed by the (0001) facet again.

High-resolution TEM (HRTEM) images were obtained from the NW tip (shown in Figure 3A) to reveal the lattice structure around the tip edges. The selected NW had a tip predominately covered by the $\{10\bar{1}3\}$ facets (Figure 3B). In general, the NW exhibited a perfect crystal lattice without any observable dislocations. No hint of screw dislocation could be identified. From the very center area, as shown in Figure 3C, a small portion (~ 3 nm) of the (0001) facet could still be observed. It quickly turned into the $\{10\bar{1}3\}$ facets with sharp corners. The lattice spacing of the $\{10\bar{1}3\}$ plane was measured to be 0.1425 nm, consistent with the JCPDS card (No. 36-1451). The $\{10\bar{1}3\}$ facets were found to be rough, as shown in Figure 3D. Islands with a few atomic layer thickness and multiple atomic steps covered almost the entire surface. This could be a result of the surface energy minimization of the crystal system.²⁹ For the same reason, the $\{10\bar{1}3\}$ facet restructured into a series of multiatomic-layer steps at the junction with the $\{10\bar{1}0\}$ facet (Figure 3E). The rough surface and corners might be responsible for the crystal facet evolution during the NW growth at different temperature and supersaturation, that is, different driving force of atom diffusion.

Above crystal lattice analysis suggested that the NWs were likely grown by a layer-by-layer mechanism, as we discovered previously.^{20,21} In this mechanism, the Ehrlich–Schwoebel (ES) barrier is a critical parameter that prevents the adatoms from diffusing over the atomic steps and thus builds up necessary adatom concentration to nucleate new atomic layers. In an ideal ZnO NW growth process, atomic layers of the

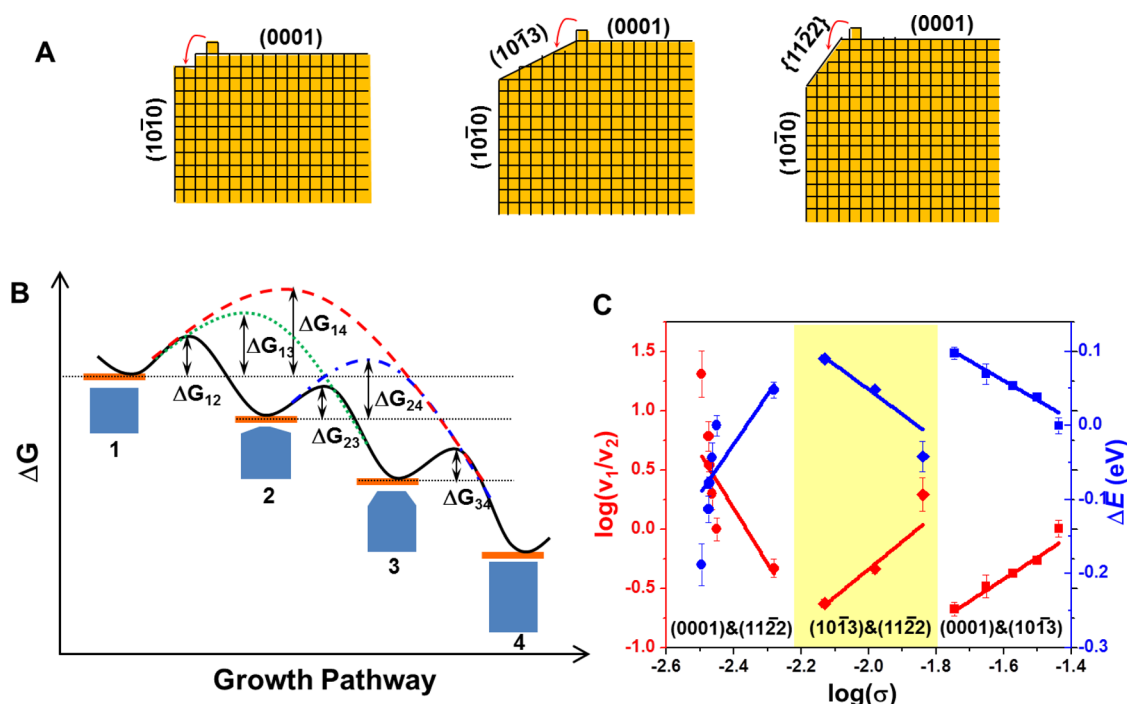


Figure 4. Analogy of facet evolution to the Ostwald–Lussac law. (A) Schematic of the facet formation model. (B) Schematic energy landscape of a series of facets illustrating the facets evolution pathway. At certain supersaturation, the high-index facets tend to be stable due to the lower energy barriers. (C) Dependence of the growth rate ratio (left, y-axis) and the energy barrier differences (right, y-axis) of (0001) and {10 $\bar{1}$ 3}, {10 $\bar{1}$ 3} and {11 $\bar{2}$ 2}, and (0001) and {11 $\bar{2}$ 2} on the supersaturation. Each dot is the average value of five sets of experimental data under the same supersaturation and the error bars represent standard deviation. The corresponding lines are fitted curves.

(0001) plane nucleate at the NW tip and grow laterally covering the entire tip surface.³⁰ Nevertheless, as the (0001) plane approaches the edge, for example, the corner with the (10 $\bar{1}$ 0) plane, new high-index crystal facets will form, such as the {10 $\bar{1}$ 3} and {11 $\bar{2}$ 2} families (Figure 4A). These facets have high surface energy and typically vanish rapidly as their sizes become appreciable (e.g., a few nanometers wide). Thus, these high-index planes can be considered as metastable intermediate stages as the complete evolution of a new (0001) plane. However, our observation of the coexistence of these high-index facets within a narrow deposition window suggested that under certain circumstances these intermediate stages might stably be present. For example, the ES barrier for adatoms to diffuse from the (0001) plane to the (10 $\bar{1}$ 3) plane might be significantly higher than that for adatoms to diffuse backward. Therefore, the overall energy barrier for the formation of a complete new (0001) plane would be much higher than that for leaving the high-energy (10 $\bar{1}$ 3) plane exposed. Similar scenario would also apply to the facets transition between the pairs of (0001)/{11 $\bar{2}$ 2} and {10 $\bar{1}$ 3}/{11 $\bar{2}$ 2} as we observed experimentally.

This free energy barrier-induced appearance of metastable intermediate stages shares much similarity with the OL law that has been primarily discovered in biomineralization.^{22–24} The OL law is an empirical law of phase transformation stating that an unstable system does not necessarily transform directly into the most stable phase, but likely into one with the minimum energy loss. Here, we propose that the crystal facet formation could also be represented by a similar energy landscape of the OL law, although the atomic plane growth is not really a phase transformation. In analogy to the OL law, a free energy landscape was constructed to show the ZnO NW tip facets evolution relationships based on our experimental observations.

As shown in Figure 4B, stage 1 to stage 4 represent the process of a complete (0001) atomic layer formation. Stage 1 represents the free energy of a NW system that is ready for growth, that is, the sum of free energies of both the NW and the supersaturated vapor phase. Stages 2–4 are the growth results that only represent the free energy of the solid NW phase. Stage 4 has the lowest free energy because of the lowest surface energy of the (0001) plane.³¹ In between stages 1 and 4, another two intermediate stages exist, for example, formation of the {10 $\bar{1}$ 3} facets (stage 2) and formation of the {11 $\bar{2}$ 2} facets (stage 3). These stages have high energy than the final stage 4 because of the higher surface energy of the high-index facets. Kinetically, the corresponding energy barriers between each stage were marked as ΔG_{ab} , where a and b represent the initial and final stage, respectively, during the crystal facet growth. As discussed previously, these energy barrier heights might change toward different directions as the ES barrier varies as a function of supersaturation.^{32,33} Under certain circumstances, the energy barriers involving intermediate stages might be significantly lower than ΔG_{14} , and thereby the high-index facets appear in the final NW morphology. The relative value between different ΔG dictates the appearing crystal facet(s). To more specifically elaborate this empirical law of facet evolution, all the experimentally observed NW tip morphology was correlated to ΔG relationships and summarized in Table 1. This table could be further enriched if more new NW tip facets are discovered.

Similar to the OL law for phase transformation, our proposed law for facet evolution at the NW growth front is purely qualitative. Quantification of all the relative energy barriers requires a comprehensive knowledge of various associated energies (e.g., the ES barrier, adsorption/desorption energy, surface energy, and so forth) and other parameters (e.g.,

Table 1. Summary of the Relationships among Coexisting Facets, Energy Barriers (ΔG_{ab}), and Morphologies

coexisting facets	ΔG relationship	morphology
(0001)	ΔG_{14} is the smallest	Figure 1I
(0001) and $\{11\bar{2}2\}$	$\Delta G_{13} < \Delta G_{12}$ and ΔG_{14}	Figure 1G,H
$\{11\bar{2}2\}$ and $\{10\bar{1}3\}$	$\Delta G_{12} < \Delta G_{13}$ and ΔG_{14} ; $\Delta G_{23} < \Delta G_{24}$	Figure 1D–F
(0001) and $\{10\bar{1}3\}$	$\Delta G_{12} < \Delta G_{13}$ and ΔG_{14} ; $\Delta G_{24} < \Delta G_{23}$	Figure 1A–C

supersaturation, vibration frequency, and so forth), which are beyond the capacity of this work. Fortunately, the facet areas demonstrated a good relation with the supersaturation. According to kinetic Wulff's theorem,³⁴ the relative growth rates of the facets can be deduced from the relative sizes of them. As discussed earlier, the supersaturation (σ) was considered as the dominating variable in correlation to the deposition location within this small window. Therefore, based on the evolved sizes of the (0001), $\{10\bar{1}3\}$, and $\{11\bar{2}2\}$ facets measured at different deposition locations, the relative growth rate was calculated and plotted as a function of σ (given by the left y -axis in Figure 4C, see Supporting Information S7.1 for σ -calculation). As the supersaturation decreased, the relative growth rate ratio of $\{10\bar{1}3\}/(0001)$ decreased from 1.02 to 0.21, and then the relative growth rate ratio of $\{11\bar{2}2\}/\{10\bar{1}3\}$ decreased from 2.38 to 0.24, and finally the relative growth rate ratio of $\{11\bar{2}2\}/(0001)$ increased from 0.45 to 31.92. The changes of relative growth rate ratio indicated that the growth energy barrier difference between the corresponding two groups of facets changed at different supersaturation.

According to the crystal growth theory,³⁵ the facet growth is linearly related to the supersaturation and exponentially related to the temperature and the growth energy barrier of corresponding facets, which can be expressed by the equation

$$v_1 = A\sigma \exp\left(-\frac{E_1}{kT}\right) \quad (1)$$

where v_1 is the growth rate of facet 1, A is a parameter related to the growth condition, E_1 is the growth energy barrier of the facet 1, k is Boltzmann constant, and T is the deposition temperature. Using this equation, the energy barrier differences were quantified as a function of σ (given by the right y -axis of Figure 4C, Supporting Information S7.2). For all of these three pairs of facets, the energy barrier difference might be fitted linearly to the logarithm of the supersaturation, indicating the energy barrier difference was logarithmically influenced by the supersaturation. At higher supersaturation level, corresponding to the location closest to the chamber center, the energy barrier for the formation of the (0001) facet was almost the same as that of the $\{10\bar{1}3\}$ facets (only ~ 1 meV difference). With the supersaturation decreased, the energy barrier of forming the (0001) facet became 96 meV larger than that of the $\{10\bar{1}3\}$ facets, confirming the rapid evolution of the $\{10\bar{1}3\}$ facets in place of the (0001) facet. Similarly, when the supersaturation continued to decrease, the energy barrier for facets $\{10\bar{1}3\}$ changed from being 50 meV smaller than that of the $\{11\bar{2}2\}$ facets to being 90 meV larger than that of the $\{11\bar{2}2\}$ facets, providing a smaller energy barrier for the facet evolution from $\{10\bar{1}3\}$ to $\{11\bar{2}2\}$. As the supersaturation decreased further, the energy barrier for (0001) formation rapidly decreased from 50 meV to -210 meV relative to the energy barrier for $\{11\bar{2}2\}$ formation, confirming a relatively larger drive force for the (0001) to quickly cover the entire NW tip, forming a flat tip surface.

In conclusion, a unique facet evolution phenomenon at the NW tip was observed at different deposition supersaturation within a narrow vapor deposition window. Electron microscopy characterization revealed that at certain conditions, high-energy crystal facets, including the $\{10\bar{1}3\}$ and $\{11\bar{2}2\}$ facets could be stably exposed at the NW tip. The relative area of these crystal facets continuously changed following the supersaturation. The facet evolution path was identified starting from the (0001) facet, then to the $\{10\bar{1}3\}$ facets, and subsequently to the $\{11\bar{2}2\}$ facets, and eventually back to the (0001) facets as the supersaturation continuously decreased. The facets evolution and exposure of high-energy facets were attributed to the fluctuation of the energy barriers for the formation of different crystal facets during the layer-by-layer growth of the NW tip. An empirical law for the NW tip facet formation was proposed in analogy to the OL law of phase transformation. That is, at appropriate deposition conditions, exposure of the crystal facets at NW growth front is not merely determined by the surface energy. Instead, the NW may choose to expose the facets with minimal formation energy barrier, which can be determined by the ES barrier variation as the supersaturation changes. On the basis of the surface area difference among different crystal facets, the energy barrier differences were quantified as a function of supersaturation. This study provides a new platform for understanding the one-dimensional or two-dimensional crystal growth kinetics, which will contribute a new insight into the controlled growth of nanostructures.

■ ASSOCIATED CONTENT

Supporting Information

The Supporting Information is available free of charge on the ACS Publications website at DOI: 10.1021/acs.nanolett.6b03317.

Experimental details, large scale SEM image, XRD, ball structure models of the facets, and calculation details about the supersaturation and growth energy barriers (PDF)

■ AUTHOR INFORMATION

Corresponding Author

*E-mail: xudong.wang@wisc.edu.

Notes

The authors declare no competing financial interest.

■ ACKNOWLEDGMENTS

The authors thank financial support from Air Force Office of Scientific Research under Award FA9550-13-1-0168.

■ REFERENCES

- (1) Lopez-Sanchez, O.; Lembke, D.; Kayci, M.; Radenovic, A.; Kis, A. *Nat. Nanotechnol.* **2013**, *8*, 497–501.
- (2) Huang, M. H.; Mao, S.; Feick, H.; Yan, H.; Wu, Y.; Kind, H.; Weber, E.; Russo, R.; Yang, P. *Science* **2001**, *292*, 1897–1899.
- (3) Kelzenberg, M. D.; Boettcher, S. W.; Petykiewicz, J. A.; Turner-Evans, D. B.; Putnam, M. C.; Warren, E. L.; Spurgeon, J. M.; Briggs, R. M.; Lewis, N. S.; Atwater, H. A. *Nat. Mater.* **2010**, *9*, 239–244.
- (4) Liu, L.; Sun, M.; Zhang, H.; Yu, Q.; Li, M.; Qi, Y.; Zhang, C.; Gao, G.; Yuan, Y.; Zhai, H. *Nano Lett.* **2016**, *16*, 688–694.
- (5) Tian, N.; Zhou, Z. Y.; Sun, S. G.; Ding, Y.; Wang, Z. L. *Science* **2007**, *316*, 732–735.
- (6) Xie, X. W.; Li, Y.; Liu, Z. Q.; Haruta, M.; Shen, W. J. *Nature* **2009**, *458*, 746–749.

- (7) Yang, X.; Shu, H.; Liang, P.; Cao, D.; Chen, X. *J. Phys. Chem. C* **2015**, *119*, 12030–12036.
- (8) Kim, F.; Connor, S.; Song, H.; Kuykendall, T.; Yang, P. D. *Angew. Chem., Int. Ed.* **2004**, *43*, 3673–3677.
- (9) Chiu, C.-Y.; Li, Y.; Ruan, L.; Ye, X.; Murray, C. B.; Huang, Y. *Nat. Chem.* **2011**, *3*, 393–399.
- (10) Liu, B.; Aydil, E. S. *J. Am. Chem. Soc.* **2009**, *131*, 3985–3990.
- (11) Vayssieres, L. *Adv. Mater.* **2003**, *15*, 464–466.
- (12) Song, J.; Kulinich, S. A.; Yan, J.; Li, Z.; He, J.; Kan, C.; Zeng, H. *Adv. Mater.* **2013**, *25*, 5750–5755.
- (13) Wulff, G. Z. *Kristallogr. - Cryst. Mater.* **1901**, *34*, 449–530.
- (14) Wu, B.; Guo, C.; Zheng, N.; Xie, Z.; Stucky, G. D. *J. Am. Chem. Soc.* **2008**, *130*, 17563–17567.
- (15) Zhang, L.; Niu, W.; Xu, G. *Nano Today* **2012**, *7*, 586–605.
- (16) Yin, A.-X.; Min, X.-Q.; Zhang, Y.-W.; Yan, C.-H. *J. Am. Chem. Soc.* **2011**, *133*, 3816–3819.
- (17) Kuo, C.-H.; Yang, Y.-C.; Gwo, S.; Huang, M. H. *J. Am. Chem. Soc.* **2011**, *133*, 1052–1057.
- (18) Jaramillo, T. F.; Jørgensen, K. P.; Bonde, J.; Nielsen, J. H.; Horch, S.; Chorkendorff, I. *Science* **2007**, *317*, 100–102.
- (19) Niu, W.; Zheng, S.; Wang, D.; Liu, X.; Li, H.; Han, S.; Chen, J.; Tang, Z.; Xu, G. *J. Am. Chem. Soc.* **2009**, *131*, 697–703.
- (20) Yin, X.; Shi, J.; Niu, X.; Huang, H.; Wang, X. *Nano Lett.* **2015**, *15*, 7766–7772.
- (21) Yin, X.; Geng, D.; Wang, X. *Angew. Chem., Int. Ed.* **2016**, *55*, 2217–2221.
- (22) Ferguson, J. *Mineral. Mag.* **1983**, *47*, 421–421.
- (23) Oswald, W. Z. *Phys. Chem.* **1897**, *22*, 289–302.
- (24) Pellegrino, E. D. *Q. Rev. Biol.* **1983**, *58*, 611–611.
- (25) Burt, D. P.; Wilson, N. R.; Weaver, J. M.; Dobson, P. S.; Macpherson, J. V. *Nano Lett.* **2005**, *5*, 639–643.
- (26) Bryce, B. A.; Ilic, B. R.; Reuter, M. C.; Tiwari, S. *Appl. Phys. Lett.* **2012**, *100*, 213106.
- (27) Greene, L. E.; Law, M.; Goldberger, J.; Kim, F.; Johnson, J. C.; Zhang, Y. F.; Saykally, R. J.; Yang, P. D. *Angew. Chem., Int. Ed.* **2003**, *42*, 3031–3034.
- (28) Xu, S.; Wei, Y.; Kirkham, M.; Liu, J.; Mai, W.; Davidovic, D.; Snyder, R. L.; Wang, Z. L. *J. Am. Chem. Soc.* **2008**, *130*, 14958.
- (29) Herring, C. *Phys. Rev.* **1951**, *82*, 87–93.
- (30) Hofmann, S.; Sharma, R.; Wirth, C. T.; Cervantes-Sodi, F.; Ducati, C.; Kasama, T.; Dunin-Borkowski, R. E.; Drucker, J.; Bennett, P.; Robertson, J. *Nat. Mater.* **2008**, *7*, 372–375.
- (31) Na, S.-H.; Park, C.-H. *J. Korea. Phys. Soc.* **2010**, *56*, 498–502.
- (32) Niu, X.; Stagon, S. P.; Huang, H.; Baldwin, J. K.; Misra, A. *Phys. Rev. Lett.* **2013**, *110*, 136102.
- (33) Tersoff, J.; Denier van der gon, A. W. D.; Tromp, R. M. *Phys. Rev. Lett.* **1994**, *72*, 266–269.
- (34) Du, D. X.; Srolovitz, D. J.; Coltrin, M. E.; Mitchell, C. C. *Phys. Rev. Lett.* **2005**, *95*, 95.
- (35) Markov, I. V. *Crystal Growth For Beginners: Fundamentals of Nucleation, Crystal Growth and Epitaxy*; World Scientific: Singapore, 2003.